ACS APPLIED ENERGY MATERIALS

Article

Cite This: ACS Appl. Energy Mater. 2019, 2, 5057−5065

www.acsaem.org

Effect of Nanosecond Laser Beam Shaping on $Cu(In,Ga)Se_2$ Thin Film Solar Cell Scribing

Seungkuk Kuk,[†] Zhen Wang,[†] Zian Jia,[†] Tao Zhang,[†] Jong-Keuk Park,[‡] Won Mok Kim,[‡] Lifeng Wang,[†] Jeung-hyun Jeong,[*,‡] and David J. Hwang[*,†]

[†]Department of Mechanical Engineering, State University of New York, Stony Brook, New York 11794, United States

[‡]Korea Institute of Science and Technology, Seoul 02792, Korea

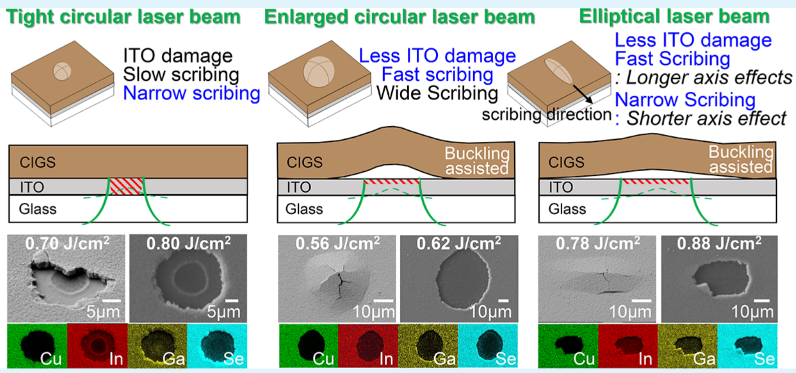

ABSTRACT: The $Cu(In,Ga)Se_2$ (CIGS) thin film solar cell is a promising material architecture considering its high photovoltaic (PV) efficiency at low material cost. Recently, the authors demonstrated all laser based mini-module fabrication on a transparent conducting oxide (TCO) based CIGS architecture, using a cost-effective nanosecond laser beam illuminated from the transparent glass substrate side. While indium tin oxide (ITO) is a promising TCO to this end, allowing ohmic contact with CIGS and low sheet resistance, it suffers from unwanted damage upon laser scribing based on its preferred thickness of ~200 nm. Therefore, in this study, we investigate the effect of laser beam size and shape on ITO damage during P2 laser scribing. Although use of an enlarged laser spot could mitigate the damage issue, larger scribing width increased the dead zone. Thus, we have implemented the elliptical laser beam shaping technology so that a longer beam axis can suppress the ITO damage also maintaining high scribing speed while a shorter beam axis dictates narrow scribing width. Based on theoretical and numerical analyses, the ITO damage free scribing trend by enlarged laser beam, at least along one laser beam axis, is attributed to the buckling mechanism that facilitates film failure by enlarged laser beam. Transient thermo-mechanical modeling results imply that larger laser beam induced thermal stress will reach the film failure threshold earlier within laser pulse duration at lower interfacial temperature. However, further time-resolved experimental investigations are necessary to find the exact film delamination timing in conjunction with possible contribution of a microexplosion mechanism.

KEYWORDS: *CIGS thin film solar cell, laser scribing, thin film scribing, nanosecond laser, elliptical beam shaping*

1. INTRODUCTION

$Cu(In,Ga)Se_2$ (CIGS) thin film photovoltaic (PV) material is a promising architecture considering its high PV efficiency at low material cost.[1] Molybdenum (Mo) has been accepted as an ideal material for bottom contact.[2] However, the opaque nature of Mo limits the laser scribing process, a preferred interconnect method; laser illumination is only available from the film side causing undesirable scribing performance in the P2 scribing process that aims to remove CIGS and upper layers for serial contacts. Upon use of cost-effective nanosecond laser solutions, the scribing process by laser illumination from the film side is mainly dictated by a thermal mechanism and augmented laser−plume interaction degrades the scribing performance.[3] Thus, use of costly ultrashort pulsed lasers has been a major solution to the scribing of Mo based CIGS PV structures.[4,5] While nanosecond lasers of near-infrared wavelengths have been examined in conjunction with tuning down the bandgap of CIGS material in order to preferentially heat up the CIGS/Mo interface,[6] such a process protocol may fundamentally limit CIGS material choices. The transparent conducting oxide (TCO) bottom contact based thin film PV allows direct laser illumination onto the absorber−TCO interface from the transparent substrate side. In such configurations, e.g., amorphous-silicon thin film PV with TCO bottom contact,[7] nanosecond lasers of visible wavelengths have been successful in launching thermal stress onto the absorber/TCO interface leading to clean removal of absorber layers with a reduced degree of phase change on the remaining structures.

Received: April 9, 2019
Accepted: June 17, 2019
Published: June 28, 2019

In earlier stage, the architecture of TCO bottom contacts has been tested for CIGS thin film PV mainly at the cell level,[8,9] and indium tin oxide (ITO) has been accepted as a promising TCO to this end, allowing ohmic contact with CIGS.[9] Recently, the authors demonstrated all the P1, P2, and P3 laser scribing processes to fabricate a mini-module on the thin film CIGS architecture with an ITO bottom contact, using a cost-effective nanosecond laser beam illuminated from the transparent glass substrate side.[10] In subsequent efforts, we have attempted to reduce the P2 and P3 scribing widths, i.e. to minimize the dead zone, for further improvement of module efficiency. However, an unfavorable trend of damaging ITO has been identified upon use of a preferred thickness of ∼200 nm. Although use of thicker ITO can mitigate the damage issue, it is not a preferred solution considering the high material cost of ITO.

In this study, we investigate the effect of laser beam size and shape on damaging the underlying TCO bottom contact during the P2 laser scribing process. All the P2 laser scribing tasks were based on a nanosecond pulsed laser with visible wavelength illuminated from transparent glass substrate side for the new CIGS PV configuration with the ITO bottom contact of ∼200 nm thickness.

2. EXPERIMENTAL PROCEDURES

As sample preparation steps for P2 laser scribing tasks, an ITO film of ∼200 nm thickness deposited on soda-lime glass (SLG) was purchased (iTASCO, Korea; ∼10 Ω/sq). Then, CIGS absorber layer of ∼2 μm thickness was first deposited on ITO by the coevaporator method, followed by deposition of CdS and i-ZnO (∼60 nm thick CdS by dip coating, ∼50 nm thick i-ZnO by sputtering). As authors previously reported,[10] use of a thicker ITO film (∼400 nm) could efficiently suppress the ITO damage via a heat spreading effect during the P2 laser scribing process. However, we proceed with a fixed ITO film thickness of ∼200 nm as a harsh condition in a fundamental sense and also for the practical purpose of keeping material cost low. Although the current study is devoted to P2 laser scribing, the results can be effectively applied to the P3 laser scribing process as very similar scribing width and threshold were confirmed in the previous works by authors because laser-induced temperature and stress profiles are not affected much by the existence of an additional top contact (AZO; Al-doped zinc oxide) when a nanosecond laser beam of 532 nm wavelength is illuminated from the SLG substrate side.[10]

For actual scribing, a nanosecond laser beam with temporal pulse width of ∼20 ns at full width half-maximum (fwhm), a fixed pulse repetition frequency of 10 kHz, wavelength of 532 nm, and laser power up to 5 W, was coupled to a galvanometric scanner combined with a telecentric f-theta lens of 100 mm focal length. Focused laser beam by the f-theta lens was irradiated onto thin films from transparent SLG substrate side, and Z linear motion stage was used to precisely adjust the laser focus by moving samples.

To adjust the laser beam from circular to elliptical shape, raw laser beam first passed through a spherical beam expander set composed of a concave and a convex spherical lens and then passed through a cylindrical beam reducer set composed of convex and concave cylindrical lenses (Figure 1). After the spherical beam expander, the circular laser beam was ∼6 mm in diameter, and after the cylindrical beam reducer, the laser beam was elliptical with shorter axis dimension of ∼1 mm while longer axis dimension was maintained at ∼6 mm. A circular laser spot ∼24 μm in diameter (1/e basis) was obtained by focusing the circular laser beam of ∼6 mm diameter by the f-theta lens. A circular beam of ∼64 μm in diameter (1/e basis) was obtained by moving samples toward the lens. An elliptical laser beam of ∼21 μm × 84 μm dimension was achieved by focusing the elliptical laser beam of ∼6 mm × ∼1 mm by the f-theta lens. Actual beam spot diameters were experimentally measured by a Gaussian fitting process based on features fabricated by various laser power levels.[11] It is noted that shorter and longer axes before focusing are reversed at laser focus because longer axes will be focused tighter due to the higher effective numerical aperture. The reduced aspect ratio of ∼4:1 at the laser focus vs ∼1:6 before focusing, was intrinsically due to nonidentical focal lengths for longer and shorter axis beams, and practically was a result of trial-and-error to find a focal plane of the maximal aspect ratio. Laser power was precisely adjusted by an external attenuator set composed of a half waveplate and polarizing beam splitter.

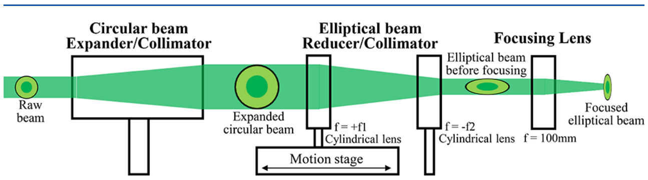

Figure 1. Schematic diagram for elliptical beam shaping.

The optical microscope (F70, Mitutoyo) and scanning electron microscope (SEM, JEOL 7600F) with energy dispersive X-ray spectroscopy (EDS) mapping function were used to inspect the morphology and elemental distribution of the scribed features. The main objective of EDS mapping is to analyze the removal of CIGS, and damage of ITO after P2 scribing. The elemental maps of Cu, Ga and Se were referred to as the indicators for the CIGS removal while the In maps served as indicators for the ITO damage.

3. THERMOMECHANICAL MODELING PROCEDURE

Thermomechanical analysis was performed to elucidate the relevant P2 scribing mechanisms, focused on the laser-induced temperature and stress evolutions for different beam sizes and shapes for a fixed laser fluence level; a circular beam of 24 μm diameter, a circular beam of 64 μm diameter, and an elliptical beam of 21 μm × 84 μm diameter. Simplified multilayer geometries of CIGS(2 μm)/ITO(200 nm)/SLG(5 μm) was simulated (Figure 2), effectively neglecting thin CdS(60 nm) and i-ZnO(50 nm) layers.

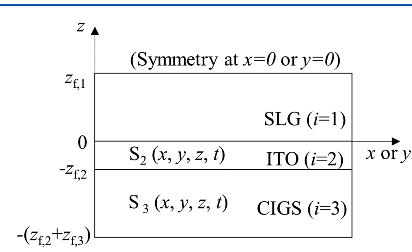

Figure 2. Geometry used for thermomechanical analysis of the P2 laser scribing process.

Three-dimensional transient heat conduction equations[10] were solved as governing equations and are shown in eqs 1−3 with heat source terms defined by eqs 4 and 5. Heat source terms were implemented in both CIGS and ITO layers based on Beer's law dependence, while they were skipped for SLG due to negligible absorption, and reflected fraction from each interface, estimated by Fresnel relation without considering the interference effect, was rejected by multiplying relevant (1-reflectivity) factors. The interference effect is negligible in terms of the ultimate laser absorption in CIGS and ITO films due to relatively small reflectivity at the interfaces involved, weak absorption by ITO, and strong absorption by CIGS. This is practically an important aspect since otherwise the laser-induced heating will be sensitively affected by the optical properties or thickness of ITO film in the current laser scribing configuration based on the SLG substrate side laser illumination. Collimated laser beam, i.e., constant laser beam spot diameter along the z-

DOI: 10.1021/acsaem.9b00717
ACS Appl. Energy Mater. 2019, 2, 5057−5065

direction, was reasonably assumed throughout multiple layers since the depth of focus of lens well exceeds the total thickness of multilayer thin films. Characteristics of pulsed laser illumination were also implemented into the heat source terms; Gaussian distribution both spatially with beam radii of 24 and 64 μm at 1/e definition, and temporally with temporal pulse width of 20 ns at fwhm. To describe the elliptical beam shape, the constant factors of a and b were implemented to determine the aspect ratio and actual beam size of the elliptical beam for x and y axis, respectively.

$$\rho_1 c_{p,1}\frac{\partial T_1(x,y,z,t)}{\partial t} = \nabla(-k_1\nabla T_1(x,y,z,t)), \quad \text{for } 0 \le z \le z_{f,1} \tag{1}$$

$$\rho_2 c_{p,2}\frac{\partial T_2(x,y,z,t)}{\partial t} = \nabla(-k_2\nabla T_2(x,y,z,t)) + S_2(x,y,z,t), \quad \text{for } -z_{f,2} \le z \le 0 \tag{2}$$

$$\rho_3 c_{p,3}\frac{\partial T_3(x,y,z,t)}{\partial t} = \nabla(-k_3\nabla T_3(x,y,z,T)) + S_3(x,y,z,t), \quad \text{for } -(z_{f,3}+z_{f,2}) \le z \le -z_{f,2} \tag{3}$$

where heat source terms are defined as

$$S_2(x,y,z,t) = (1-R_2)(1-R_1)\frac{2}{\tau_p}\left(\frac{\ln 2}{\pi}\right)^{1/2}F_{av}\exp\left(-4\ln 2\left(\frac{t^2}{\tau_p{}^2}\right)\right)a_2\exp(-a_2|z|)\exp\left(-\frac{\left(\frac{x}{a}\right)^2+\left(\frac{y}{b}\right)^2}{w_0{}^2}\right) \tag{4}$$

$$S_3(x,y,z,t) = (1-R_3)(1-R_2)(1-R_1)\frac{2}{\tau_p}\left(\frac{\ln 2}{\pi}\right)^{1/2}F_{av}\exp\left(-4\ln 2\left(\frac{t^2}{\tau_p{}^2}\right)\right)a_3\exp(-a_3(|z|-z_{f,2}))\exp(-a_2 z_{f,2})\exp\left(-\frac{\left(\frac{x}{a}\right)^2+\left(\frac{y}{b}\right)^2}{w_0{}^2}\right) \tag{5}$$

where τ_p, F_{av}, and w_0 are laser pulse duration at fwhm, laser fluence (J/m^2), and laser beam radius irradiated on film (1/e definition), respectively. a_i, ρ_i, $c_{p,i}$, and k_i are absorption coefficient, density, specific heat, and thermal conductivity of i-layer, respectively (i denotes an index for each material layer; 1 for SLG, 2 for ITO, and 3 for CIGS). a and b are factors to determine the aspect ratio and size of the elliptical beam as mentioned earlier. R_1, R_2, and R_3 are reflectivity for Air/SLG, SLG/ITO, and ITO/CIGS interfaces, respectively.

A lateral domain size of 150 μm × 150 μm and 5 μm thickness for SLG was set to apply the effective semi-infinite boundary conditions at locations far from a laser spot, considering thermal diffusion length scale of the order hundreds of nanometers within nanosecond laser pulse duration for materials composing the simulation geometry. Convective and radiative losses through the CIGS film top were neglected by applying adiabatic boundary conditions, and no thermal contact resistances were considered at interfaces by applying continuous temperature and heat flux boundary conditions. The initial condition was set at room temperature in all the locations. The simulated time range was between −20 and 20 ns with setting time zero at the peak laser intensity timing for the laser pulse duration of 20 ns at fwhm. Quarter spatial domain was simulated based on symmetric boundary conditions to reduce computational load. Due to difficulty in finding thermal, mechanical, and optical properties of composing materials that strongly depend on temperature and deposition process, representative room temperature properties available in the literature were used (refer to Table 1).[6,12−15]

Coupled with the heat equation, laser-induced thermal stress was calculated by the stress−strain relationship given in the following[16,17]

$$\sigma = D\varepsilon_{elast} = D(\varepsilon - \varepsilon_{th}) \tag{6}$$

where σ, ε_{elast}, ε, ε_{th}, and D is stress, elastic strain, total strain, thermal strain, and elasticity of materials, respectively. Stress and strain vectors were composed of six components as shown below

$$\sigma = \begin{bmatrix}\sigma_{xx}\\ \sigma_{yy}\\ \sigma_{zz}\\ \sigma_{xy}\\ \sigma_{xz}\\ \sigma_{yz}\end{bmatrix}, \quad \varepsilon = \begin{bmatrix}\varepsilon_{xx}\\ \varepsilon_{yy}\\ \varepsilon_{zz}\\ \varepsilon_{xy}\\ \varepsilon_{xz}\\ \varepsilon_{yz}\end{bmatrix} = \begin{bmatrix}\frac{\partial u_x}{\partial x}\\ \frac{\partial u_y}{\partial y}\\ \frac{\partial u_z}{\partial z}\\ \left[\frac{\partial u_x}{\partial y}+\frac{\partial u_y}{\partial x}\right]\\ \left[\frac{\partial u_x}{\partial z}+\frac{\partial u_z}{\partial x}\right]\\ \left[\frac{\partial u_y}{\partial z}+\frac{\partial u_z}{\partial y}\right]\end{bmatrix},$$

$$\varepsilon_{th} = \frac{1}{3}\begin{bmatrix}\alpha(T-T_{room})\\ \alpha(T-T_{room})\\ \alpha(T-T_{room})\\ 0\\ 0\\ 0\end{bmatrix} \tag{7}$$

The elasticity matrix (D) was composed of elastic modulus (E) and Poisson's ratio (ν), and isotropic material properties were assumed. The elasticity matrix can be simplified to eq 8 by using Lame's constants of μ and λ defined in terms of elastic modulus and poison's ratio (eq 9)

DOI: 10.1021/acsaem.9b00717
ACS Appl. Energy Mater. 2019, 2, 5057−5065

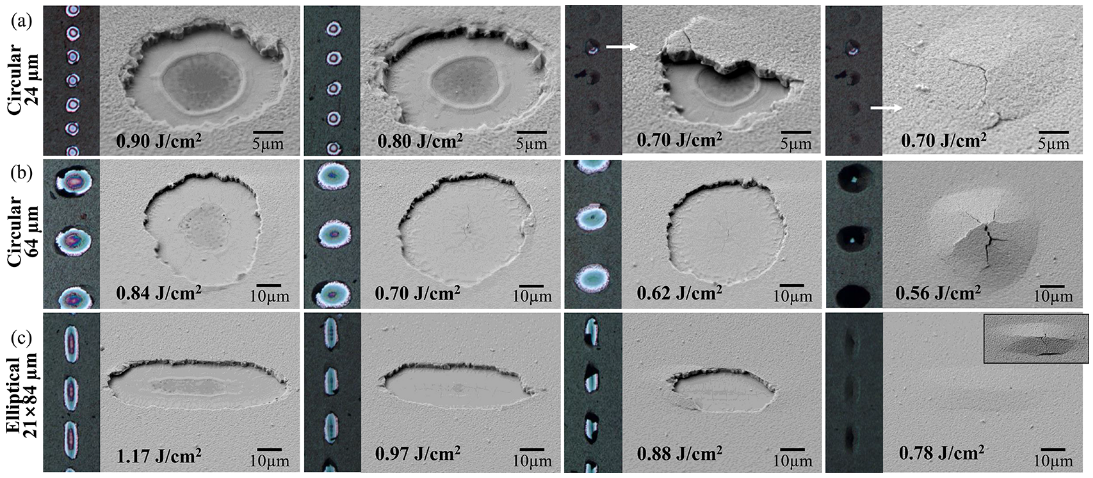

Figure 3. Single laser shot based P2 scribing results by (a) 24 μm diameter circular beam, (b) 64 μm diameter circular beam, and (c) 21 μm × 84 μm elliptical beam. An optical microscope and a 30° tilted SEM image are shown for each condition with laser fluence marked.

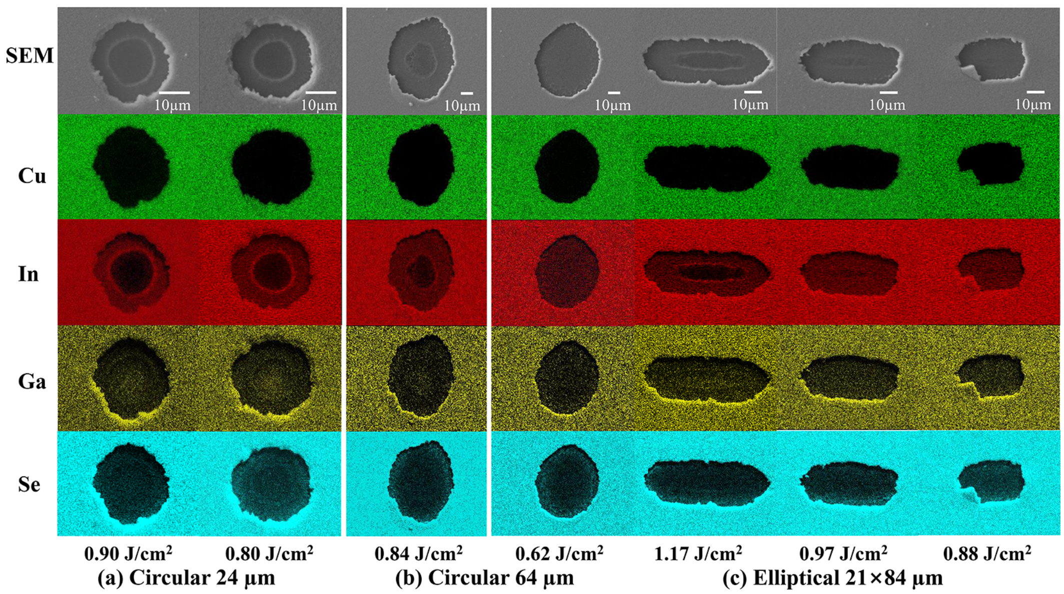

Figure 4. EDS elemental mapping analysis results for single laser shot based P2 scribing by (a) circular beam 24 μm diameter, (b) circular beam of 64 μm diameter, and (c) 21 μm × 84 μm elliptical beam with laser fluence marked for each scribing condition.

$$D = \begin{bmatrix} \lambda + 2\mu & \lambda & \lambda & 0 & 0 & 0 \\ \lambda & \lambda + 2\mu & \lambda & 0 & 0 & 0 \\ \lambda & \lambda & \lambda + 2\mu & 0 & 0 & 0 \\ 0 & 0 & 0 & \mu & 0 & 0 \\ 0 & 0 & 0 & 0 & \mu & 0 \\ 0 & 0 & 0 & 0 & 0 & \mu \end{bmatrix} \tag{8}$$

$$\mu = \frac{E}{2(1 + v)}, \quad \lambda = \frac{Ev}{(1 + v)(1 - 2v)} \tag{9}$$

For boundary conditions, we assumed zero stress and strain at locations far from the laser heated spots, free boundary condition at CIGS surface, $z = -(z_{f,3} + z_{f,2})$, and fixed boundary conditions for all other boundaries. As the initial condition, zero stress was assumed before laser illumination.

4. EXPERIMENTAL RESULTS

The main objective of the P2 scribing is to selectively remove the stack of i-ZnO/CdS/CIGS without damaging the underlying ITO and without inducing intermetallic diffusion of CIGS components to the exposed ITO so that the efficient electrical paths to connect bottom (ITO) and top contacts (AZO) can be provided. Enabled by the optical transparency of ITO bottom contact, P2 scribing was possible by SLG substrate side laser illumination via thermal stress launched at the CIGS/ITO interface. The choice of 532 nm wavelength (photon energy ~2.3 eV) was a balance between high transparency through SLG and ITO, and strong absorption in CIGS regardless of the bandgap tuning of CIGS. Figures 3 and 4 show selected results of single laser shot based P2 scribing by different beam sizes and shapes with varying laser fluences.

By the circular beam of 24 μm diameter, it was very difficult to avoid the ITO damage although relatively small scribing size of ~24 μm was achievable at the scribing threshold of ~0.8 J/cm^2 as seen from SEM images in Figure 3a. The EDS based In

DOI: 10.1021/acsaem.9b00717
ACS Appl. Energy Mater. 2019, 2, 5057−5065

elemental maps in Figure 4a confirm significant ITO material loss and also visualize the trace of Ga diffusion into the damaged ITO spots. Even at 0.7 J/cm^2, corresponding to the fluence below CIGS scribing threshold, serious damage is observed on partly exposed ITO. On the contrary, the circular beam of 64 μm diameter noticeably suppressed the ITO damage, especially at the threshold fluence of ~0.62 J/cm^2 as confirmed by SEM images in Figure 3b and the EDS maps in Figure 4b. The scribing threshold was reduced by 64 μm circular beam. However, a large scribing spot size of ~47 μm (at the scribing threshold fluence of 0.62 J/cm^2) was a major issue due to the increased dead zone. In order to address the aforementioned issues of circular beam, elliptical beam shaping has been implemented so that the longer axis activates the effect of enlarged beam suppressing the ITO damage while the shorter axis dictates narrow scribing width by scanning in parallel to the longer axis for the P2 scribing. As observed in SEM images in Figure 3c and elemental maps in Figure 4c, the P2 scribing by a 21 μm × 84 μm elliptical beam indeed suppressed the ITO damage while narrow scribing widths are formed along the shorter axis. The scribing width remained almost constant at small dimension of ~20−22 μm regardless of laser fluences. However, the enlarged scribing length along the longer axis sensitively changed with varying degrees of ITO damage. By 1.17 J/cm^2, the aspect ratio of the scribed spot is almost identical to that of the elliptical beam (4:1) yet with noticeable ITO damage. As laser fluence decreased to 0.97 and 0.88 J/cm^2, the aspect ratio of the scribed spot gradually reduced with a lesser degree of ITO damage and intermetallic diffusion. It is an obvious trend that an elliptically shaped laser beam can produce narrow P2 scribing features with minimized ITO damage.

Further insights on the film delamination trends can be obtained from the incomplete scribing cases in Figure 3, corresponding to the fluences just below scribing thresholds, i.e., 0.7 J/cm^2 for 24 μm circular beam, 0.56 J/cm^2 for 64 μm circular beam, and 0.78 J/cm^2 for a 21 μm × 84 μm elliptical beam. A 24 μm circular beam led to a lesser degree of film bulging possibly due to the relatively stiffer nature of a smaller deformation region involved. On the contrary, the film deformation by 64 μm circular beam shows a clearly larger degree of bulging even by significantly lower laser fluence, implying that the film deformation is governed by different mechanism(s) for an enlarged region of effectively lower stiffness.

We believe that the buckling mechanism facilitates the deformation process for the enlarged laser beam cases as discussed further in a later section. The degree of film bulging by a 21 μm × 84 μm elliptical beam was limited possibly due to the constraining effect of the shorter beam axis. However, it is obvious that the longer axis facilitates the CIGS film delamination with suppressed ITO damage. Fracture preferentially found at the edges along the shorter axis seems to be a consequence of easier deformation along the longer axis; once noticeable deformation occurs mainly along the longer axis, the edges of the shorter beam axis will be subjected to increased stress due to its stiffer nature.

Table 1. Thermal, Optical, and Mechanical Properties of Materials Used for Numerical Analysis

properties	unit	glass[12]	ITO[13]	CIGS[6,12,14,15]
thermal conductivity, κ	W/mK	1	11	37
density, ρ	kg/m^3	2500	7110	5770
heat capacity, c_p	J/(kg K)	830	370	300
refractive index (n, k)		(1.525, 8.97 × 10^{-7})	(1.777, 0.00478)	(3.0964, 0.592)
absorption coefficient, α	1/m	~0	1.1291 × 10^5	2 × 10^7
Young's modulus, E	Gpa	70	116	75
Poisson index		0.2	0.35	0.4
thermal expansion, β	10^{-6} K^{-1}	9	6.37	10

Toward practical scribing line patterns, series of laser pulses were applied with varying degrees of pulse overlap precisely adjusted by laser scanning speed control. Figure 5 summarizes the P2 line scribing results by a few selected scanning speeds and laser fluences. As expected, scribing lines based on the 24 μm circular beam and its single shot scribing threshold fluence of 0.8 J/cm^2 caused severe damage of ITO regardless of pulse overlap control although narrow scribing width of ~24 μm was achievable by scribing at 100−200 mm/s, as observed from the SEM images in Figure 5a and the EDS based elemental maps in Figure 6a. Reduced laser fluence of 0.7 J/cm^2, lower than the single shot scribing threshold, could not remove the film.

On the other hand, the 64 μm circular beam could produce scribing lines of acceptable quality by properly overlapping the single shot threshold condition of 0.62 J/cm^2 (Figure 3b). High scribing speed up to 450 mm/s was achieved since larger unit scribing spots were overlapped. The EDS maps shown in Figure 6b verify the minimized ITO damage, but the trace of Se, as CIGS residues, is noticed within the scribed region mainly at the peripheral regions of individual shots, which is a negative aspect possibly increasing the contact resistance. Use of 0.56 J/cm^2, corresponding to a fluence lower than the single shot scribing threshold, produced a reasonable scribing line at a lower speed of 400 mm/s. In general, with the circular beam of 64 μm diameter, high quality removal of the CIGS was possible without damaging ITO. However, a large scribing width of ~47 μm (at the scribing threshold fluence of 0.62 J/cm^2) leading to the enlarged dead zone, and CIGS residues that will increase the contact resistance were the main issues of 64 μm circular beam. Largely deformed scribing edges are also noticed due to the softer nature of the larger deformation area involved, which could be potential sources of device instability.

Figure 5c shows representative P2 scribing lines by 21 μm × 84 μm elliptical beam. Dictated by the dimension of the shorter axis, the scribing width was ~20−22 μm regardless of laser fluence and scribing speed. Assisted by the extended beam dimension along the longer axis, higher scribing speeds up to 600 mm/s were achieved by 0.88 J/cm^2. However, laser fluence and scribing speed had to be tuned down to suppress the ITO damage to the minimal degree, and in fact the ITO damage trend is consistent with single shot scribing results (Figure 3c). At the fluence of 0.88 J/cm^2, a scribing speed up to 500 mm/s was achieved as shown in Figure 5c, which is a significant improvement vs 100−200 mm/s by 24 μm circular beam that produced similarly small scribing width. Scribing speed was also improved when compared with ~450 mm/s by the circular beam of 64 μm, implying that the partially delaminated edges at both ends of the longer axis facilitated film removal process at the overlapped sites to a certain degree. It is also seen that the P2 scribing was possible by the laser fluence (0.78 J/cm^2) lower than the single shot scribing threshold (0.88 J/cm^2). Such a trend was found only for an enlarged beam at least along one axis. The EDS analysis results shown in Figure 6c confirm

DOI: 10.1021/acsaem.9b00717
ACS Appl. Energy Mater. 2019, 2, 5057−5065

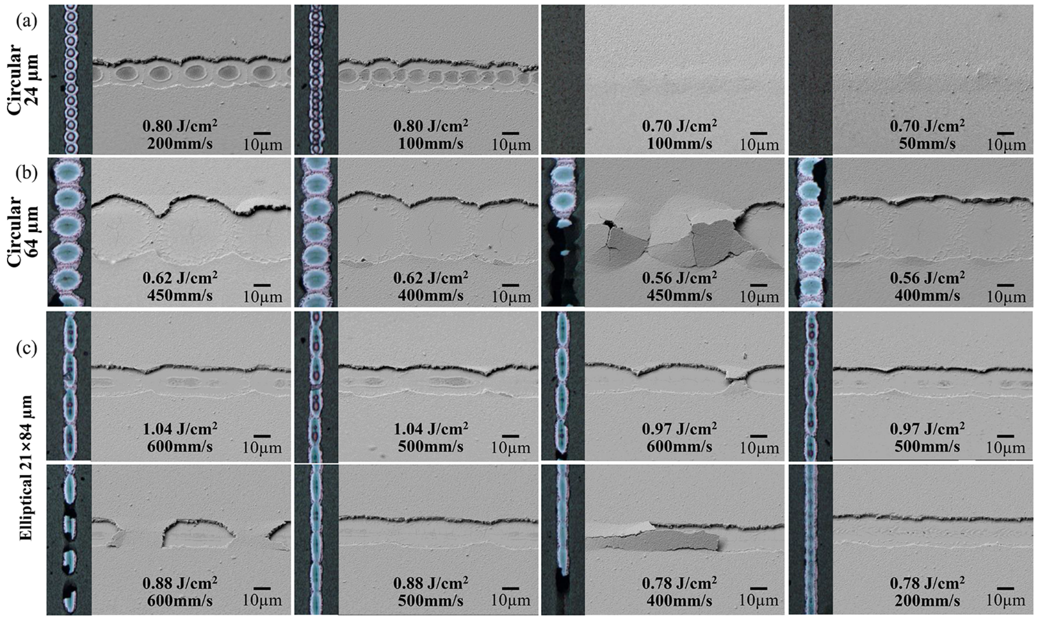

Figure 5. P2 line scribing results by (a) 24 μm diameter circular beam, (b) 64 μm diameter circular beam, and (c) 21 μm × 84 μm elliptical beam. An optical microscope and a 30° tilted SEM image are shown for each condition with laser fluence and scribing speed marked.

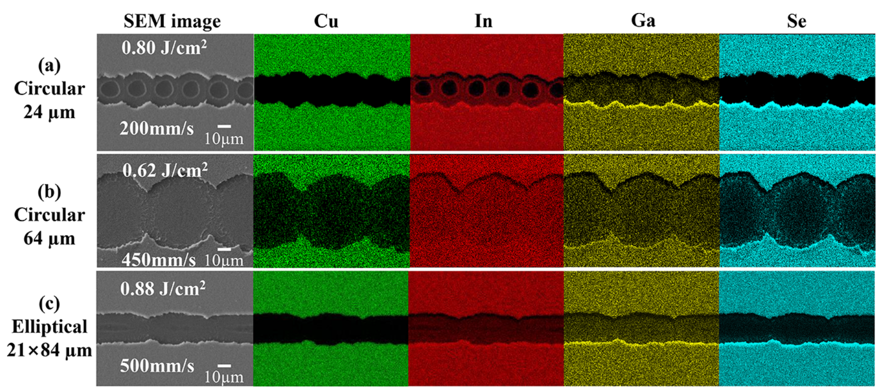

Figure 6. EDS elemental mapping analysis results for P2 scribing lines by (a) circular beam 24 μm diameter, (b) circular beam of 64 μm diameter, and (c) 21 μm × 84 μm elliptical beam, by laser fluence and scribing speed marked for each scribing condition.

minimized ITO damage, and interestingly the CIGS residues are barely found within the scribed region, which is a highly favorable aspect in terms of minimizing the P2 contact resistance.

Frequently, the P2 scribing performance is evaluated by measuring contact resistance after depositing top contact layer such as AZO. Such top contact deposition process can compensate the ITO material loss by the P2 scribing process, implementing the artifact in strictly evaluating the P2 scribing performance. It is true that such compensation effect is also expected in actual module fabrication process, indicating a relatively forgiving nature of the P2 process. In this context, more important requirement for the P2 scribing process will be to minimize unwanted intermetallic diffusion of CIGS components onto top of ITO bottom contact to keep contact resistance low. It should be noted that the ITO damage is accompanied by significant intermetallic diffusion at high CIGS−ITO interface temperature and/or molten state. Considering all the aspects explained, we decided to mainly rely on the SEM/EDS analysis to evaluate P2 performance rather than measuring contact resistance.

5. THERMOMECHANICAL ANALYSIS RESULTS

As an attempt to further explore different scribing mechanisms depending on beam size and shape, we consider the cases with similar fluence levels at around 0.9 J/cm^2 from experimental results in Figure 3; the circular beam of 24 μm diameter caused serious ITO damage by 0.8−0.9 J/cm^2 while ITO damage was greatly suppressed by the circular beam of 64 μm diameter with fluence of 0.84 J/cm^2, and the elliptical beam of 21 μm × 84 μm dimension with 0.88 J/cm^2. In parallel, in order to obtain further insights, thermomechanical simulations were also performed with an identical laser fluence of 0.88 J/cm^2 for circular beam of 24 μm diameter, circular beam of 64 μm diameter, and an elliptical beam of 21 μm × 84 μm dimension as selected results are summarized in Figure 7.

In the current P2 configuration, the substrate side laser illumination will mainly heat up the CIGS−ITO interface, launching thermal stress and/or activating microexplosion mechanisms. CIGS is directly heated up by absorbed laser energy while ITO is mainly heated by conductive heat transfer from CIGS due to weak absorption of laser energy by ITO. Considering that the lateral thermal diffusion is negligible (beam

DOI: 10.1021/acsaem.9b00717
ACS Appl. Energy Mater. 2019, 2, 5057−5065

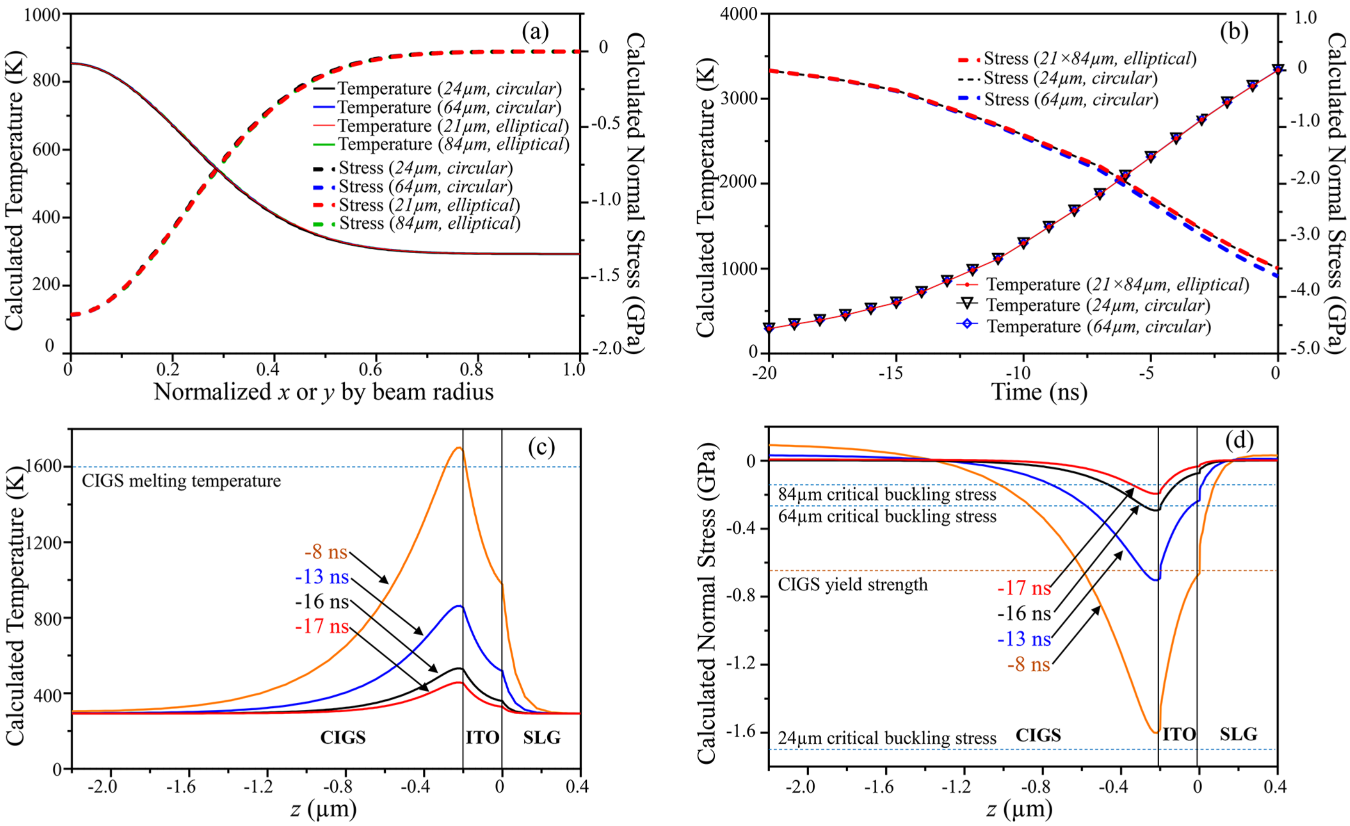

Figure 7. Calculated temperature and stress profiles for P2 scribing by a fixed fluence of 0.88 J/cm^2 for different beam sizes and shapes; circular beam of 24 μm diameter, circular beam with 64 μm diameter, and elliptical beam of 21 μm × 84 μm dimension. A normal stress component in x or y direction are plotted to show stress distribution. (a) Lateral temperature profile at CIGS−ITO interface and −13 ns for different laser beam sizes and shapes, x or y scale was normalized by respective radius, (b) temperature evolution at $x = y = 0$ and CIGS−ITO interface, zero time corresponds to peak intensity timing of laser pulse, (c) depth profile of temperature at $x = y = 0$ and CIGS−ITO interface for different timings, and (d) depth profile of stress at $x = y = 0$ and CIGS−ITO interface for different timings.

sizes of tens of micrometers ≫ lateral thermal diffusion length of 100s nm), the temperature profile along normalized lateral domain will be very similar for all three cases with the identical film thicknesses. The stress profile will be also very similar since thermal stress originates from laser-induced temperature profile. The negative sign for stress values denotes compressive components, and normal stress components along the x or y direction are plotted. Figure 7a shows the lateral temperature and stress distributions along x and y scales normalized by respective beam radius at the CIGS−ITO interface and −13 ns timing, confirming that similar temperature and stress evolutions anticipated. The temporal evolution of peak temperature and stress plotted in Figure 7b is also very similar for different beam sizes and shapes until laser peak intensity timing (zero time) as expected. The location of peak temperature and stress was at the beam center ($x = y = 0$) and near the CIGS−ITO interface in z direction. A slight shift of z location of peak temperature/stress from the CIGS−ITO interface, as seen from depth profiles in Figure 7c and d, is due to conductive heat loss through the ITO layer. Thus, the temperature and stress profiles cannot directly explain the different scribing behaviors. Even for the case the micro-explosion mechanism is involved via preferential heating of CIGS in contact with ITO, there is no specific reason why higher pressure can be induced by larger laser beam based on an identical fluence (i.e., energy per area).

A clue is found when film failure thresholds are taken into consideration; although compressive yield strength is independent of beam size,[18] the buckling threshold, i.e., the critical buckling stress as described by eq 10,[19] has strong dependence on the beam size; a larger disk with the same thickness tends to be softer and reaches the buckling threshold more easily. Buckling has been accepted as one of the thin film delamination mechanisms. The relaxation of compressive stress in the region of the detached thin films is represented as buckling, while the underlying material system stays undeformed.[1] The critical buckling stress (σ_b) is expressed as follows:[19]

$$\sigma_b = -\frac{\pi^2 E_f}{12}\left(\frac{h_f}{r_b}\right)^2 \tag{10}$$

where E_f, h_f, and r_b denote Young's modulus, film thickness, and radius of deformed area, respectively. The radius of the deformed area roughly corresponds to the laser beam radius in this study. Typical compressive yield strength of thin film CIGS is ∼0.64 GPa, independent of beam size,[18] while the critical buckling stress varies depending on the beam size; ∼1.7 GPa for the circular beam of 24 μm diameter, ∼0.24 GPa for the circular beam of 64 μm diameter, and ∼2.2 and ∼0.14 GPa along the shorter and longer axes of the 21 μm × 84 μm elliptical beam, respectively. Therefore, during the laser-induced transient heating process, thermal stress built up at the CIGS−ITO interface will continue to grow over time, and film failure may be initiated upon reaching a lower failure threshold depending on beam size and shape; the circular beam of 24 μm diameter will first reach the compressive yield strength of ∼0.64 GPa while the

DOI: 10.1021/acsaem.9b00717
ACS Appl. Energy Mater. 2019, 2, 5057−5065

circular beam of 64 μm diameter and the elliptical beam with longer axis of 84 μm should reach the critical buckling stress of ~0.37 and ~0.2 GPa, respectively. Thermal stress generated within the CIGS film can be evaluated by the approximate solution of the thermoelasticity problem for a round plate with fixed edges[7]

$$\sigma_{\max} = E\alpha T/(2(1-\nu)) \quad (11)$$

where a Young's modulus (E) of ~110 GPa, thermal expansion coefficient of ~10^{-5} K^{-1} (α), and Poisson ratio of ~0.34 (ν) can be taken from the literature for CIGS,[6] and temperature difference along the radius (ΔT) is relative to a temperature of 300 K in the surrounding region. The estimated temperatures at laser beam center to reach different threshold stresses by eq 11 are 1068 K to reach a yield strength of 0.64 GPa for 24 μm circular beam, 588 K to reach a critical buckling stress of 0.24 GPa for 64 μm circular beam, and 468 K to reach critical buckling stress of 0.14 GPa for elliptical with 84 μm longer axis. Therefore, heating of the CIGS film by a larger beam can reach failure strength at significantly lower temperature, or in much earlier stages of laser-induced heating, considering similar evolution of temperature and stress for different beam sizes and shapes of similar fluence as explained in Figure 7b. Information on such time dependent temperature and stress evolution can be obtained from thermomechanical simulation results in Figures 7c and d. Laser-induced thermal stress first reaches 0.14 GPa, the critical buckling stress across the longer axis of an elliptical beam (84 μm dimension) at −17 ns with peak temperature of 457 K; next it reaches 0.24 GPa, the critical buckling stress for 64 μm circular beam at −16 ns with peak temperature of 532 K; and last is 0.64 GPa, the yield strength for the 24 μm circular beam at −13 ns with a peak temperature of 863 K. The numerically calculated temperatures are lower than those of eq 10 implying that heating into further depth of the film (vs interface only) is necessary to reach the film failure threshold. Although the actual film delamination time is not clear because stress for a deeper portion of the CIGS layer will have to exceed respective failure stress levels, the simulation results reasonably support that a larger beam will induce CIGS delamination at shorter time scales at lower CIGS/ITO interface temperature, thus suppressing the ITO damage.

As explained above, the buckling mechanism is a unique path facilitating film failure for larger beam cases. However, the actual delamination of CIGS off from ITO will be also assisted by the microexplosion of CIGS materials at the CIGS−ITO interface upon laser illumination from the substrate side, and it has been reported that such a microexplosion mechanism still enables clean film removal minimally affecting underlying film or substrate due to the favorable plasma expansion trend.[7,20] Again, the complexity is in that it is not clear how fast the film delamination can occur. The delamination timing is important because unless the CIGS film is delaminated at a certain timing within pulse duration, the CIGS/ITO interface temperature can exceed a melting temperature of CIGS or ITO (~1600 K for CIGS and ~1900 K for ITO),[12] as shown from the calculated peak temperature evolution in Figure 7c. Also, if the delamination event is not fast enough, a molten/evaporated CIGS or ITO based microexplosion can play a role. Once CIGS is delaminated from ITO within laser pulse duration, temperature increase in the ITO film will stop. Time-resolved imaging was recently performed for a Mo film scribing process by ultrafast laser beam illuminated from substrate side[21] indicating that the timing of film delamination can be as early as a few nanoseconds after laser illumination. Thus, it is likely that larger beam based P2 scribing in this study will induce earlier CIGS film delamination at given fluence level possibly within laser pulse duration (~40 ns span from a laser pulse with fwhm temporal width of 20 ns). Under this situation, i.e. delamination of CIGS based on lower CIGS-ITO interface temperature at early timing within the pulse duration, it can be effectively assumed that the deformation or delamination of the underlying ITO film will be suppressed. This hypothesis is also supported by strong adhesion of ITO with the glass substrate and higher stiffness and melting temperature of ITO vs CIGS, as a basis of launching the buckling mechanism mainly onto the CIGS film leaving the ITO minimally affected by the larger beam. CIGS can be continuously heated up even after delamination by continuously absorbing laser energy, ultimately reaching states of higher temperature and/or phase change and thus film fracture.

6. FURTHER DISCUSSION

In general, the ITO bottom contact based CIGS architecture has enabled cell efficiency exceeding ~16%, which is just ~1−2% lower than Mo based counterpart mainly due to higher serial resistance thus also resulting in lower fill factor (vs similar open circuit voltage and short circuit current), attributed to the high resistance of ITO. As we believe that the module design with reduced unit cell width can be a possible solution, the minimization of dead zone is very important, which is the major impact anticipated from narrower P2 (and P3) scribing width enabled in current study. The ITO forms Ohmic contact with CIGS, maintaining stabile device characteristics at high temperature up to ~550 °C. As CIGS was deposited at 450 °C in current study, the unwanted reaction at ITO−CIGS interface is efficiently suppressed, and any product of minor interface reaction can be removed by the P2 laser scribing as confirmed by EDS mapping results. With carrier concentration of the order of 10^{20} cm^{-3} or higher, contact between AZO (top contact) and ITO should be efficient under this circumstance. Currently, we are making further efforts for the optimal module fabrication through additional tasks including the optimal P3 scribing process free from ITO damage and shunt through scribing edges and the optimal tuning of CIGS composition. The demonstrated damage-free scribing performance by the elliptically shaped laser beam can be effectively applied to a wider range of application fields including other types of thin film PVs including amorphous silicon, CdTe (cadmium telluride) and perovskite, and touchpad or display devices.

7. CONCLUSION

In summary, we investigated the effect of the laser beam size and shape on damaging the underlying ITO during P2 laser scribing based on a nanosecond pulsed laser of 532 nm wavelength illuminated from substrate side for new CIGS configuration with ITO thickness of 200 nm as the bottom contact. By a circular laser beam of 24 μm diameter, it was very difficult to avoid ITO damage although a relatively small scribing width of ~24 μm was achieved. A circular beam of 64 μm diameter noticeably suppressed ITO damage with reduced scribing threshold fluence and improved scribing speed. However, a large scribing spot size of ~47 μm and CIGS residues found within scribed region were negative aspects in terms of PV efficiency. In order to address the issues of enlarged circular beam, the elliptical beam shaping technique was applied; longer axis was to suppress ITO damage

DOI: 10.1021/acsaem.9b00717
ACS Appl. Energy Mater. 2019, 2, 5057−5065

and maintain high scribing speed by taking advantage of enlarged beam while shorter axis was to dictate narrow scribing width by scanning along longer axis. Using a 21 μm × 84 μm elliptical beam suppressed the ITO damage simultaneously maintaining narrow scribing line of ~20−22 μm width along shorter axis, and also the CIGS residues were minimized within the scribed region.

Based on theoretical and numerical calculations, it is believed that a favorable trend of removing CIGS and upper layers without ITO damage by larger laser beam at least along one axis, is related to the buckling based film failure mechanism. While the compressive yield strength is independent of beam size, the critical buckling stress has strong dependence on the beam size, and for larger beam within tested range, the critical buckling stress is smaller than the compressive yield strength. Transient thermo-mechanical modeling results indicate that the larger beam reaches a failure threshold earlier within laser pulse duration at lower interfacial temperature as a supporting trend to suppress the underlying ITO damage. However, further time-resolved experimental investigations are necessary to find the exact timing of CIGS delamination off from the ITO, interface temperature, and phase of contacting layers at that timing in relation to the contribution of the microexplosion.

■ AUTHOR INFORMATION

Corresponding Authors

*Email: jhjeong@kist.re.kr.

*Email: david.hwang@stonybrook.edu.

ORCID

Lifeng Wang: 0000-0002-2068-5102

Jeung-hyun Jeong: 0000-0003-0147-5158

David J. Hwang: 0000-0002-9928-1484

Notes

The authors declare no competing financial interest.

■ ACKNOWLEDGMENTS

The authors acknowledge the support from Korea Institute of Energy Technology Evaluation and Planning (KETEP) and the Ministry of Trade, Industry & Energy (MOTIE) of the Republic of Korea (20158520000060). This work was also supported by the internal program of the Korea Institute of Science and Technology (Project No. 2E29510). This work was partly supported by the Technology Development Program to Solve Climate Changes of the National Research Foundation (NRF) funded by the Ministry of Science, ICT & Future Planning (2016M1A2A2936782) of Republic of Korea. This research used resources of the Center for Functional Nanomaterials, which is a U.S. DOE Office of Science Facility, at Brookhaven National Laboratory under Contract No. DE-SC0012704.

■ REFERENCES

(1) Chirila, A.; Reinhard, P.; Pianezzi, F.; Bloesch, P.; Uhl, A. R.; Fella, C.; Kranz, L.; Keller, D.; Gretener, C.; Hagendorfer, H.; Jaeger, D.; Erni, R.; Nishiwaki, S.; Buecheler, S.; Tiwari, A. N. Potassium-induced surface modification of Cu(In,Ga)Se2 thin films for high-efficiency solar cells. *Nat. Mater.* **2013**, *12*, 1107−1111.

(2) Gecys, P.; Markauskas, E.; Nishiwaki, S.; et al. CIGS thin-film solar module processing: case of high-speed laser scribing. *Sci. Rep.* **2017**, *7*, 40502.

(3) Hermann, J.; Benfarah, M.; Bruneau, S.; Axente, E.; Coustillier, G.; Itina, T.; Guillemoles, J. F.; Alloncle, P. Comparative investigation of solar cell thin film processing using nanosecond and femtosecond lasers. *J. Phys. D: Appl. Phys.* **2006**, *39*, 453−460.

(4) Gecys, P.; Raciukaitis, G.; Ehrhardt, M.; Zimmer, K.; Gedvilas, M. Ps-laser scribing of CIGS films at different wavelengths. *Appl. Phys. A: Mater. Sci. Process.* **2010**, *101*, 373−378.

(5) Nishiwaki, S.; Burn, A.; Buecheler, S.; Muralt, M.; Pilz, S.; Romano, V.; Witte, R.; Krainer, L.; Spuhler, G. J.; Tiwari, A. N. A monolithically integrated high-efficiency Cu(In,Ga)Se_2 mini-module structured solely by laser. *Prog. Photovolt: Res. Appl.* **2015**, *23*, 1908−1915.

(6) Lee, S. H.; Kim, C. K.; In, J. H.; Shim, H. S.; Jeong, S. H. Selective removal of Cu In_{1-x} Ga_x Se_2 absorber layer with no edge melting using a nanosecond Nd:YAG laser. *J. Phys. D: Appl. Phys.* **2013**, *46*, 105502.

(7) Bovatsek, J.; Tamhankar, A.; Patel, R. S.; Bulgakova, N. M.; Bonse, J. Thin film removal mechanisms in ns-laser processing of photovoltaic materials. *Thin Solid Films* **2010**, *518*, 2897−2904.

(8) Nakada, T. Microstructural and diffusion properties of CIGS thin film solar cells fabricated using transparent conducting oxide back contacts. *Thin Solid Films* **2005**, *480−481*, 419−425.

(9) Nakada, T.; Hirabayashi, Y.; Tokado, T.; Ohmori, D.; Mise, T. Novel device structure for Cu(In,Ga)Se_2 thin film solar cells using transparent conducting oxide back and front contacts. *Sol. Energy* **2004**, *77*, 739−747.

(10) Kuk, S.; Wang, Z.; Fu, S.; Zhang, T.; Yu, Y.; Choi, J.; Jeong, J.; Hwang, D. Nanosecond laser scribing of CIGS thin film solar cell based on ITO bottom contact. *Appl. Phys. Lett.* **2018**, *112*, 134102.

(11) Liu, J. M. Simple technique for measurements of pulsed Gaussian-beam spot sizes. *Opt. Lett.* **1982**, *7*, 196.

(12) Buzas, A.; Geretovszky, Z. Nanosecond laser-induced selective removal of the active layer of CuInGaSe2 solar cells by stress-assisted ablation. *Phys. Rev. B: Condens. Matter Mater. Phys.* **2012**, *85*, 245304.

(13) Medvedovski, E.; Alvarez, N.; Yankov, O.; Olsson, M. K. Advanced indium-tin oxide ceramics for sputtering targets. *Ceram. Int.* **2008**, *34*, 1173−1182.

(14) Hermann, J.; Benfarah, M.; Bruneau, S.; Axente, E.; Coustillier, G.; Itina, T.; Guillemoles, J. F.; Alloncle, P. Comparative investigation of solar cell thin film processing using nanosecond and femtosecond lasers. *J. Phys. D: Appl. Phys.* **2006**, *39*, 453−460.

(15) Bae, S.; Zhao, H.; Hsieh, Y.; Zuo, L.; Marco, N.; Rim, Y.; Li, G.; Yang, Y. Printable Solar Cells from Advanced Solution-Processible. *Materials Chem.* **2016**, *1*, 197−219.

(16) Jackson, P.; Wuerz, R.; Hariskos, D.; Lotter, E.; Witte, W.; Powalla, M. Effects of heavy alkali elements in Cu(In,Ga)Se2 solar cells with efficiencies up to 22.6%. *Phys. Status Solidi RRL* **2016**, *10*, 583−586.

(17) Timoshenko, S. P.; Goodier, J. N. *Theory of Elasticity*; Mcgraw-hill, 1951.

(18) Luo, S.; Lee, J. H.; Liu, C. W.; Shieh, J. M.; Shen, C. H.; Wu, T. T.; Jang, D.; Greer, J. R. Strength, stiffness, and microstructure of Cu(In,Ga)Se2 thin films deposited via sputtering and co-evaporation. *Appl. Phys. Lett.* **2014**, *105*, 011907.

(19) Freund, I. B.; Suresh, S. *Thin film Materials: Stress, Defect Formation and Surface Evolution*; Cambridge University Press, 2003.

(20) Wang, H.; Hsu, S.; Tan, H.; Yao, Y. L.; Chen, H.; Azer, M. N. Predictive Modeling for Glass-Side Laser Scribing of Thin Film Photovoltaic Cells. *J. Manuf. Sci. Eng.* **2013**, *135*, 051004.

(21) Domke, M.; Rapp, S.; Schmidt, M.; Huber, H. Ultra-fast movies of thin-film laser ablation. *Appl. Phys. A: Mater. Sci. Process.* **2012**, *109*, 409−420.

DOI: 10.1021/acsaem.9b00717
ACS Appl. Energy Mater. 2019, 2, 5057−5065